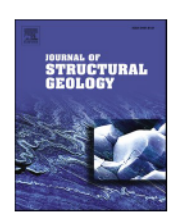
ELSEVIER

Contents lists available at ScienceDirect

# Journal of Structural Geology

journal homepage: www.elsevier.com/locate/jsg





# Effects of coseismic megasplay fault activity on earthquake hazards: Insights from discrete element simulations

Xiaoyu Wang<sup>\*</sup>, Julia Morgan

Department of Earth, Environmental and Planetary Sciences, Rice University, Houston, TX, USA

#### ARTICLE INFO

Keywords:
Megasplay fault
Discrete element
Numerical simulation
Tsunami potential
Megathrust earthquake

#### ABSTRACT

Deep-water megasplay faults may promote or limit earthquake rupture and tsunami genesis. To better understand how megasplay faults affect earthquake rupture and associated tsunami potential, we use the Discrete Element Method (DEM) to model the upper plate as a wedge that is partitioned into a seismic (velocity-weakening, VW) inner wedge and an aseismic outer (velocity-strengthening, VS) wedge, combined with a splay fault rooting at the decollement. We examine the effects of the width of the outer (VS) wedge, as well as the dip and friction along the splay fault during earthquake rupture. Our results suggest that along-strike variations in the width of the VS outer wedge along the Chile Margin may play a key role in splay fault activity in the ruptured segment of the 2010 Maule earthquake. In addition, our model fit to the published slip distribution for the 2010 Maule earthquake suggests that megasplay fault activation did not significantly impact earthquake size along the south-central Chile Margin. In contrast, our model fit to the slip distribution for the 2011 Tohoku earthquake shows that megasplay fault reactivation may have moderately affected earthquake coseismic rupture. Splay faults can slip coseismically, contributing to associated tsunamis. However, the presence of a VS outer wedge is the predominant constraint on rupture size and tsunami generation.

# 1. Introduction

Pre-existing forearc structures may influence the seismic hazard potential (Bécel et al., 2017; Olsen et al., 2020; Polet and Kanamori, 2000; Wang and Tréhu, 2016). Key features include deep-water megasplay faults, which branch upward from a megathrust plate interface and may extend up to the seafloor (Lieser et al., 2014; Melnick et al., 2012; Park et al., 2002). The megasplay faults are often characterized by steep dips and can be reactivated during large coseismic ruptures, contributing to the generation of transoceanic tsunamis (Lotto et al., 2019; Moore et al., 2007; Wendt et al., 2009). The conditions under which megasplay faults promote or limit earthquake rupture and tsunami genesis, however, are still unclear.

Thrust megasplay fault systems may act as barriers to seismic rupture. As an example, the activation of the thrust-type Santa Maria thrust fault system (SMFS) at Isla Santa Maria in south-central (SC) Chile, may have contributed to segmenting and limiting finite megathrust slip during the Mw 8.8 2010 Maule earthquake, which had an epicenter about 20 km away (Melnick et al., 2006, 2012; Tong et al., 2010). In contrast, normal megasplay faults may facilitate earthquake

rupture and tsunami generation. One example is the apparent reactivation of a normal fault within the upper plate during the Mw 9.0 2011 Tohoku earthquake (Ito et al., 2011; Tsuji et al., 2011). The tsunami that accompanied that event caused severe damage along the coastline of Japan. The uplift and seaward displacement of the footwall of the splay normal fault may have contributed to the large horizontal displacement along the megathrust (McKenzie and Jackson, 2012; Tsuji et al., 2011). Thus, the sense of fault slip (i.e., normal or thrust) may control both earthquake size and tsunami potential. This hypothesis, however, is not well understood and has not yet been carefully tested.

A structural configuration comparable to the one involved in the Tohoku earthquake is interpreted in the Shumagin Gap, offshore Alaska, where a normal-type megasplay fault may have been activated by seismic ruptures propagated from adjacent locked segments (Bécel et al., 2017). The activation of the normal fault may have caused the large historic tsunami in the Shumagin Gap. Interestingly, Mw 7.8 Simeonof and Mw 8.2 Chignik earthquakes recently occurred in the vicinity of the Shumagin Gap in July 2020 and July 2021, respectively, with epicenters close to that configuration. In contrast to the Tohoku earthquake, these two events only caused waves of less than a foot (Grassi, 2021; Ruppert

E-mail addresses: xiaoyu.wang@ifb.baug.ethz.ch (X. Wang), morganj@rice.edu (J. Morgan).

<sup>\*</sup> Corresponding author.

#### and Gardine, 2021).

One potential controlling factor that may contribute to the difference between the tsunami genesis for the Tohoku earthquake and the recent Alaska earthquakes is the variation in properties of a pre-existing megasplay fault, including fault dip and effective friction coefficient. The dip may control the uplift of the seafloor and the coseismic rupture due to the complex stress interactions between the main fault and splay faults (Kame et al., 2003; Wendt et al., 2009). The effective friction coefficient along the megasplay fault may determine the activation of the megasplay fault, which may modulate the amount of slip on the megathrust fault (Lotto et al., 2019). Furthermore, the geometric and mechanical properties of the splay fault that can affect the earthquake and tsunami size may vary along the strike, influencing the activity of the splay fault during and after the mainshock. A possible demonstration of this effect is along the SC Chile Margin, where forearc splay faults were activated by the great 2010 Maule earthquake in some segments of the rupture zone but not in adjacent ones (Lieser et al., 2014).

Another plausible controlling factor that may affect the earthquake size, tsunami size, or splay fault activations are variations in effective friction coefficient along the megathrust fault (Cubas et al., 2013; Wang and Morgan, 2019; Wang et al., 2021). Previous studies have shown correlations between the widths of outer wedges, which are presumed to slip aseismically due to the velocity strengthening (VS) rheology of the underlying megathrust, and the coseismic ruptures and stress transfer triggered by great megathrust earthquakes (Contreras-Reyes et al., 2010; Lotto et al., 2017; Wang et al., 2021). In contrast, the megathrust beneath the seismic inner wedge experiences velocity-weakening (VW) behavior that enables earthquake rupture and inner wedge extension. The presence of a VS outer wedge induces compressive stress at the aseismic/seismic transition zone, which suppresses the propagation of the coseismic ruptures (Wang and Hu, 2006; Wang et al., 2021). This coseismic stress transfer may influence the sense of slip and the degree of reactivation along a pre-existing megasplay fault in an offshore forearc.

To assess the local seismic hazard, therefore, it may not be enough simply to determine the presence and properties of a megasplay fault, as we also must understand how outer wedge width controls the activation and sense of slip along the megasplay fault during a seismic event. Here, we build on previous numerical simulations of megathrust slip processes (Wang et al., 2021) to examine the role of splay faults within the upper plate. Motivated by the Dynamic Coulomb Wedge model (Wang and Hu, 2006), we use the numerical Discrete-Element-Method (DEM) to simulate a two-dimensional upper plate driven by displacement of a rigid backwall. This study aims to 1) investigate the factors (i.e., friction conditions along megathrust and splay fault, dips) that control the activation and sense of slip (i.e., normal or thrust) of a splay fault; 2) better understand how splay faults influence fault displacement and tsunami generation; and finally, 3) explore the role of fault reactivation in determining the earthquake size and tsunami potential for the 2010 Maule and 2011 Tohoku earthquakes.

#### 2. Approach and methodology

#### 2.1. Initial geometry and mechanical properties

The program code, RICEBAL, is used for the DEM simulations, and details about the DEM methodology can be found in the previous publications (Morgan, 2015; Wang and Morgan, 2019). We build on recent modeling efforts that focused on observations of extensional deformation in the Japan Trench forearc and Chile Margin (Wang et al., 2021).

The initial wedge is constructed by randomly generating particles within a two-dimensional domain and allowing them to settle under gravity (Fig. 1). The assemblage of compacted particles is then sculpted into the desired wedge shape with a starting taper angle of  $10^{\circ}$  ( $\alpha+\beta$ ), and subjected to gravity tilted at an angle of  $8^{\circ}$  from the vertical, simulating a fixed megathrust dip angle ( $\beta$ ) of  $8^{\circ}$ . The geometry of the upper plate is simplified as a triangular wedge in its initial state, and the sliding surface underlying the wedge (in green in Fig. 1) is the simulated planar megathrust plate boundary. This reference configuration is comparable to published geometries for several subduction margins (Ito et al., 2011; Maksymowicz, 2015; Wang et al., 2019). The initial full width of the wedge is 200 km, consistent with a typical downdip rupture distance along the subduction margin (Moreno et al., 2010, 2012; Wei et al., 2012). Focusing on the first-order effects of megasplay fault properties on earthquake rupture and tsunami potential during an

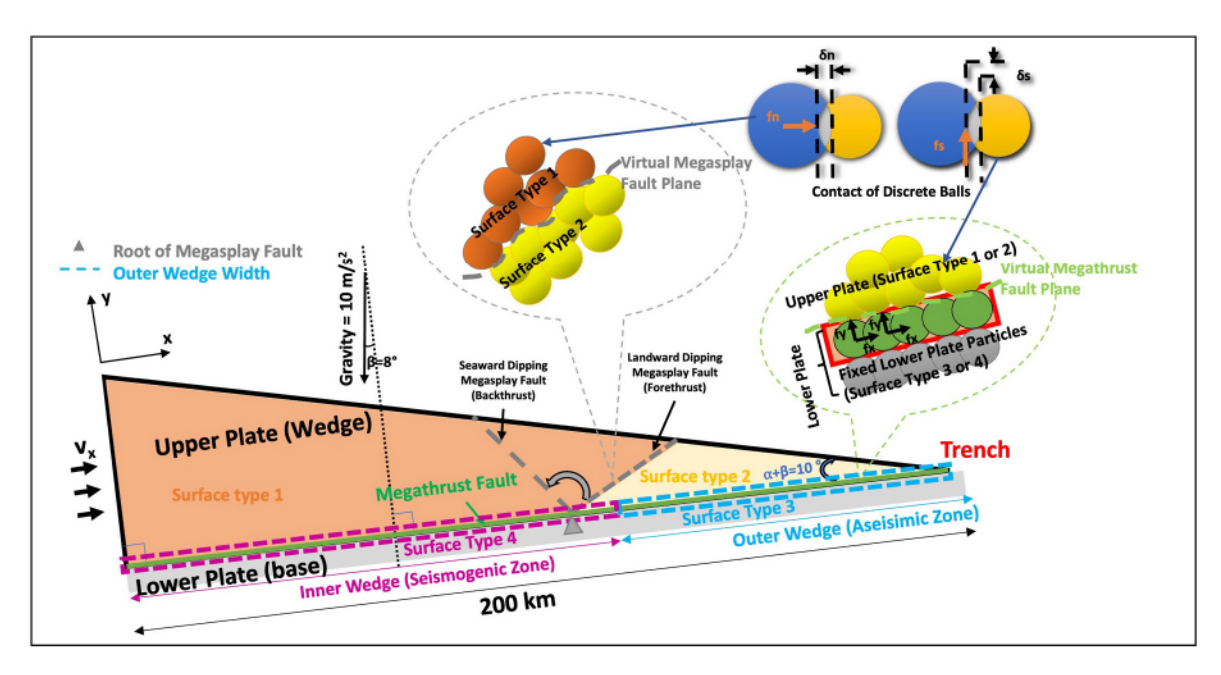


Fig. 1. DEM Model Setup. The lower plate in gray is fixed, while the upper plate in orange or yellow moves above it. The virtual splay fault plane (black line) is defined by prescribing different interparticle friction coefficients at contacts, and the plane dip can be varied and pre-defined. The backwall moves along the megathrust fault plane at a constant rate of  $v_x = 1$  m/s during the pre-earthquake stage, but wall displacement ceases ( $v_x = 0$  m/s) during the earthquake unloading stage. Details about the particle contacts and surface type pre-assignments can be found in the supplementary material (Table S1 and Text S2). (For interpretation of the references to color in this figure legend, the reader is referred to the Web version of this article.)

earthquake cycle, we employ constant values of basal friction across each inner wedge or outer wedge for a given simulation stage, ignoring the spatial and temporal variations that likely occur in nature. The friction coefficients along the megasplay fault (denoted by green lines in Fig. 1) are also constant for a given simulation stage. To clearly investigate certain controlling factors, our simplified model employs a sharp updip transition at the inner and outer wedge boundary. Details about the setup and the preset parameters can be found in the supplemental materials (Text S1, Table S1, and Table S2).

# 2.2. Boundary conditions and simulation workflow

Each numerical simulation is carried out in two stages: preearthquake loading and dynamic rupture (Fig. S1). We note that the downdip boundary of the upper plate is defined as a rigid boundary of the wedge, on which a constant rate of wall displacement introduces compression parallel to the megathrust fault plane. This displacement is applied during the pre-earthquake loading stage, simulating the far-field tectonic displacement. Thus, we do not simulate variations in fault slip downdip of this boundary, which defines the downdip limit of the seismogenic zone. The colored yellow and orange particles within the wedge are free to rotate and move, while the colored green and gray particles, defining the basal sliding surface, are fixed in space (Fig. 1).

During the first loading stage, the backwall is displaced at a steady rate, while the megathrust slip of the wedge is resisted by constant basal friction. This causes the build-up of elastic strain energy within the wedge and increased shear stresses along the megathrust. Stage 1 is terminated following 8 km of backwall displacement, at which point the fault is poised for failure. The 8 km of backwall displacement is analogous to the slip accumulated during multiple earthquake cycles.

The second stage is to simulate the dynamic weakening to trigger earthquake unloading. The framework of rate-and-state friction (RSF) provides empirical relations among the measured friction coefficient, slip rate, and slip state, where the parameter (a - b) characterizes the velocity-dependence of friction coefficient at steady-state, with a > b resulting in velocity-strengthening (VS) aseismic fault segments and a < b resulting in velocity-weakening (VW) seismogenic fault segments (Dieterich, 1979; Scholz, 1998). The relationship among pore pressure ratio, the value of a-b, and frictional strength have been derived by laboratory experiments of the fault rock composition for the subduction zones at the hydrothermal conditions (Okamoto et al., 2020; Rabinowitz et al., 2018; Ujiie et al., 2013). In our unloading Stage 2, we do not explicitly apply RSF to simulate the dynamic rupture but instead directly manipulate the value of the interparticle friction coefficient assigned along the decollement to simulate dynamic weakening and strengthening of the fault during the earthquake. This provides us with direct control on the onset of the earthquake unloading. The instantaneous reduction in basal friction along the decollement (Fig. S1a in supplemental materials) is similar to the change from static to dynamic friction during an earthquake (Rabinowicz, 1951). More information about the modeling workflow can be found in the supplemental materials (Text S2 and Fig. S1) and our previous work (Wang and Morgan, 2019; Wang et al., 2021). Before the dynamic rupture stage, we introduce a megasplay fault with a prescribed dip, ranging from landward (forethrust) to seaward (backthrust) dipping (gray dashed lines in Fig. 1). For each simulation, we assign one of four values of friction along the megasplay faults to assess the effect. Then, to simulate velocity weakening during coseismic rupture (Stage 2), the basal friction is instantly decreased beneath the inner wedge, resulting in dynamic slip along the underlying fault. Concurrently, the basal friction beneath the outer wedge is maintained at a higher value, simulating a more resistant frontal wedge. Changes in geometry and stress in the system are documented through Stage 2 until the fault slip ceases.

#### 2.3. Experimental design and different model setups

Two sets of simulations are carried out to address two specific objectives: Setup 1 uses non-cohesive wedges to investigate possible controls on splay fault activation and seafloor uplift. In particular, the simulations examine whether the width of the outer wedge (VS zone) influences the reactivation and sense of slip along pre-existing splay faults of different orientations. Setup 2 investigates the effects of both landward and seaward dipping splay faults with specific orientations on coseismic slip distributions and seafloor uplift. This fault configuration builds upon our previous study that used non-faulted cohesive wedges to reproduce the published slip distributions for the 2010 Maule earthquake and the 2011 Tohoku earthquake (Wang et al., 2021). Here, we assess if the presence of splay faults, as interpreted by others (Melnick et al., 2006; Tsuji et al., 2011), yields significantly different slip distributions that might affect the coseismic rupture and tsunami potential for both the 2010 Maule rupture zone and the 2011 Tohoku rupture zone.

To demonstrate the effect of the splay fault slip during the earthquake specifically, we introduce the fault prior to the dynamic rupture stage (Stage 2). Although we could also prescribe the splay faults before the preconditioning stage (Stage 1), they would accumulate different deformation and stress levels during loading, and thus each model would accumulate different elastic strain energy before Stage 2, making it difficult to specifically examine the effect of the splay fault activity during the seismic event.

# 2.3.1. Setup 1: effects of outer wedge width and splay fault orientation

In our first experimental setup, non-cohesive models are constructed with pre-existing splay faults with different orientations, all of which root into the decollement at 50 km distance from the toe. Fault orientations range from  $10^\circ$  to  $60^\circ$  with landward dips, and  $20^\circ - 80^\circ$  with seaward dips. Outer wedge widths range from 0% to  $\sim\!25\%$  of the full wedge length. In all models, the internal friction coefficient  $(\mu'_{int})$  was maintained at 0.30 for both the inner and outer wedges (Table S1). The effective basal friction coefficients for the inner and outer wedges,  $\mu'_{bas\_inner}$  and  $\mu'_{bas\_outer}$ , respectively, were both set to 0.10 at the start of the pre-earthquake loading stage. During the earthquake rupture phase,  $\mu^{\prime}_{bas\_inner}$  was instantly decreased to 0.00 while  $\mu^{\prime}_{bas\_outer}$  was maintained at 0.10. In all models, the splay fault is introduced just before earthquake unloading, allowing us to test the impact of coseismic slip along the fault on the earthquake size and surface deformation. Simulation results are compared to a reference model without a prescribed megasplay fault.

2.3.2. Setup 2: effects of fault friction on prescribed splay fault orientations The second experimental setup examines the effects of a splay fault on coseismic displacements and seafloor uplift for models designed based on structural interpretations for the 2010 Maule earthquake and 2011 Tohoku earthquake (Melnick et al., 2012; Tsuji et al., 2011). To define more realistic properties for these systems, cohesion was introduced by adding bonds at the contacts among particles within the initial wedge following particle deposition and wedge sculpting. We employ the same mechanical parameters as in our previous study here (Wang et al., 2021), which defined realistic configurations for these two settings. The friction coefficients prescribed to the models (Table S1) are based on our previous simulations (Wang et al., 2021) and other studies (Dielforder, 2017; Fulton et al., 2013; Wang and Hu, 2006) that constrained the strength of the megathrust and forearc in both the Maule and Tohoku areas. As above, the splay faults are introduced into the models just before earthquake unloading. The Maule models employ a seaward dipping fault of 80°, which is positioned based on the seismic interpretation of Melnick et al. (2006). A range of fault friction coefficients between 0.00 and 0.10 was tested. The Tohoku models use a landward dipping fault of 30°, located based on the interpretations of (Tsuji et al., 2011), again using the same range of fault friction values as

above. The widths of the high friction (VS) outer wedge were fixed for these models to match those used previously (Wang et al., 2021), set to ~90 km from the toe for the Maule models and less than 5 km from the toe for Tohoku models in the initial model setups.

#### 3. Results

#### 3.1. Effect of outer wedge width on stress transfer and splay fault activity

The first set of simulations using Setup 1 examined the effects of the width of the aseismic outer wedge (VS zone) on stress transfer and splay fault activity (Figs. 2 and 3). Landward dipping splay faults (forethrust) or seaward dipping splay faults (backthrust) oriented at 45° are introduced just prior to earthquake unloading using different outer wedge widths ranging from 0% to 25% of the full wedge width. Stress transfer during earthquake unloading was determined by differencing the mean stress  $(\sigma_m)$  field from pre- to post-earthquake. We refer to this as the cumulative change in  $\sigma_m$  (Fig. 2a–d, and Fig. 3a–d). The corresponding distortional strain invariant field is also examined for each simulation to observe the internal deformation (Fig. 2e–h and 3e to 3h). Details about how the  $\sigma_m$  and the distortional strain invariant fields are calculated can be found in our previous studies (Morgan, 2015; Wang and Morgan, 2019).

# 3.1.1. Landward dipping megasplay (forethrust) fault activity

The final states of simulations with the 45° landward dipping splay fault are plotted in Fig. 2. As shown in Fig. 2a–d,  $\sigma_m$  within the inner wedge decreases (shown in intensifying shades of blue, i.e., cold color) during the earthquake, whereas  $\sigma_m$  rises (intensifying shades of red, i.e., warm color) in the region of the VS outer wedge (azure dashed line)

close to the transition zone. As the ratio of the outer wedge (VS zone) width to the full wedge length decreases from 25% to less than 1% (from Fig. 2a–d), the area of increased  $\sigma_m$  (warm color regions in Fig. 2a–d) progressively decreases, demonstrating that the narrower the VS outer wedge, the easier it is for coseismic ruptures to propagate to the toe.

The cumulative distortional invariant plots, shown in Fig. 2e–h, exhibit a corresponding trend, reflected in variations in displacement along the splay fault with decreasing outer wedge width. The splay fault favors thrust faulting when there is a large outer wedge (Fig. 2e) but exhibits normal displacement when the outer wedge width is very small (Fig. 2g and h). The presence of the resistant outer wedge constrains the coseismic rupture and wedge extension during the earthquake unloading, and concurrently influences the sense of slip along the megasplay fault. In general, Fig. 2e–h shows a progressive transition from a thrust sense of slip to a normal sense of slip.

The orientation of the maximum principal stress  $(\sigma_1)$  is also calculated and plotted for  $1.5~km\times1.5~km$  element to track the stress rotation in the wedge (Fig. S2 in supplemental materials). The  $\sigma_1$  vector and cumulative change in  $\sigma_m$  are plotted together. Fig. S2a shows the initial state of the wedge, which is the reference state for each case that experiences earthquake unloading (Figs. S2b–S2e). At the initial state (before the earthquake unloading), the  $\sigma_1$  vectors are inclined to the decollement, demonstrating a compressive stress regime due to the frictional resistance to sliding. During the earthquake unloading (Figs. S2b–S2e), the  $\sigma_1$  vector rotates to subvertical within the inner wedge in response to the weakened fault beneath it, indicating stress drop (cold color region).

We also plot the  $\sigma_1$  vector with the final distortional strain invariant field (Figs. S2f–S2j) for the regions highlighted by gray boxes in Figs. S2a–S2e. Comparing the initial state (Fig. S2f) with the final state

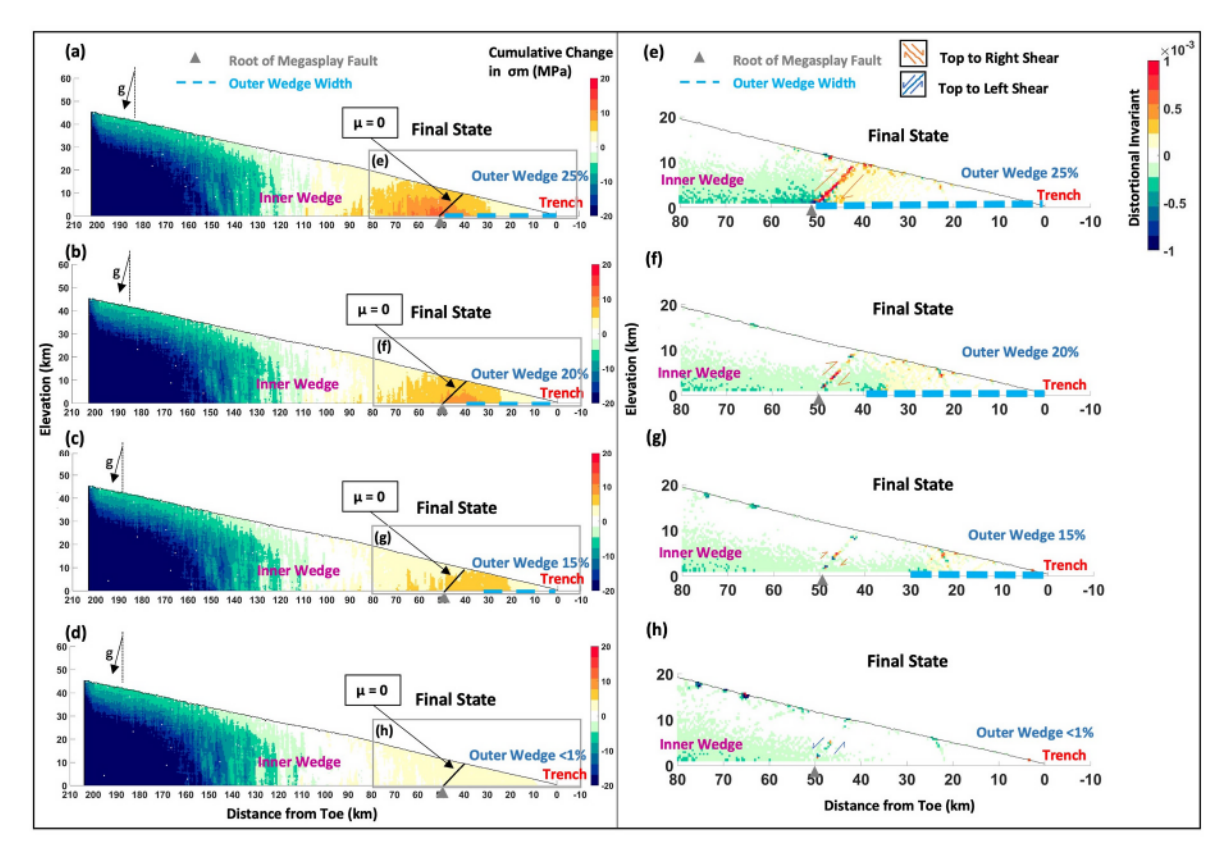


Fig. 2. Effect of outer wedge width on stress and strain in models with  $45^{\circ}$  landward dipping splay fault with friction coefficients of zero. (a)–(d) Simulated coseismic changes in mean stress  $(\sigma_m)$  field for each earthquake, denoting stress transfer within wedge; red indicates an increase in mean stress  $(\sigma_m)$ ; blue indicates a decrease. (e)–(h) Final cumulative distortional strain invariant field for each case. Black lines indicate splay fault boundaries. Azure dashed lines represent a range of outer wedges. Gray triangles indicate roots of splay faults. (For interpretation of the references to color in this figure legend, the reader is referred to the Web version of this article.)

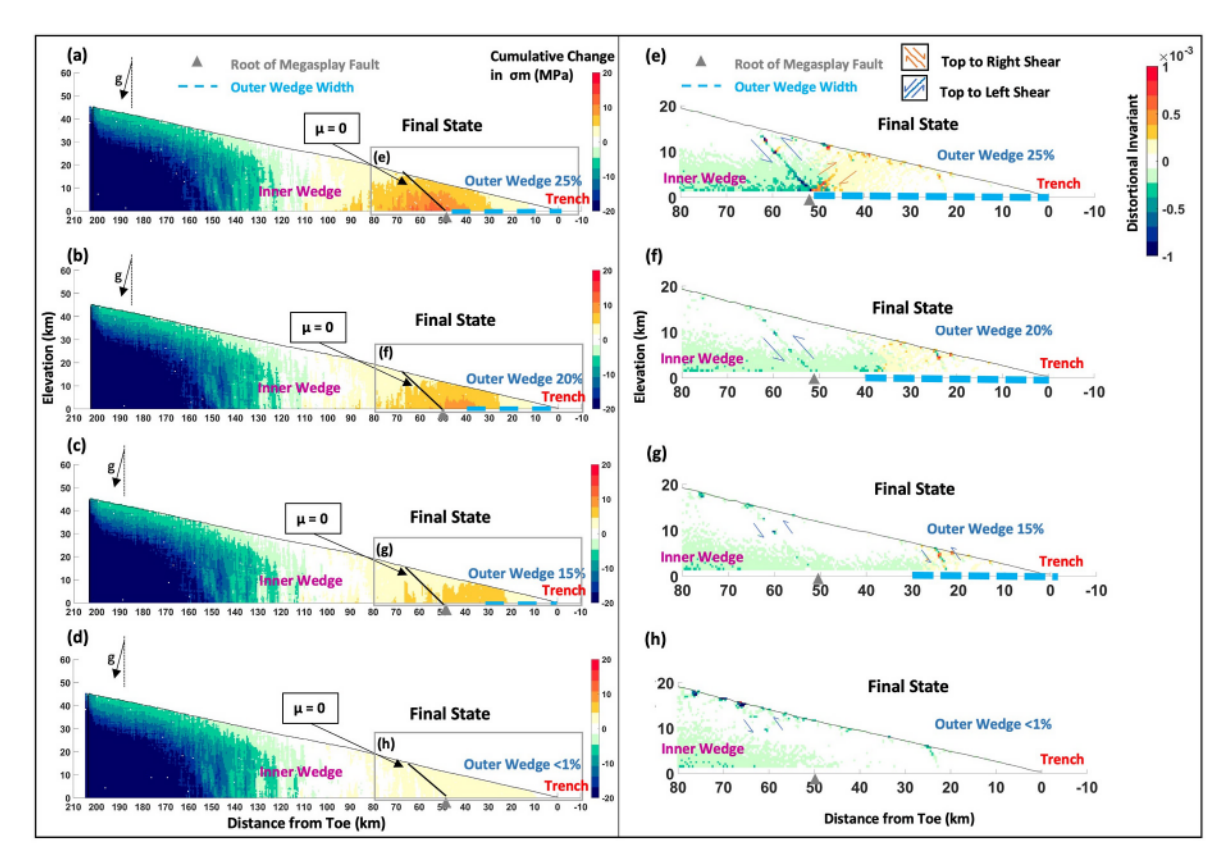


Fig. 3. Effect of outer wedge width on stress and strain in the model with 45° seaward dipping splay fault. (a)–(d) Simulated coseismic changes in mean stress (σ<sub>m</sub>) field for each earthquake. (e)–(h) Final cumulative distortional strain invariant field for each case. Colors and symbols are the same as in Fig. 2. (For interpretation of the references to color in this figure legend, the reader is referred to the Web version of this article.)

of each case (Figs. S2g–S2j), we see that in cases with large widths of the velocity-strengthening outer wedge, the  $\sigma_1$  vectors remain inclined within the toe of the wedge (Figs. S2g and S2h), whereas in cases with very small outer wedges, the  $\sigma_1$  vectors are very small and nearly horizontal, indicating nearly complete unloading of the wedge toe (Figs. S2i and S2j). We do not see sharp transitions across the megasplay faults (areas highlighted by red circles in Figs. S2g–S2j), which indicates that the faults do not cause significant stress partitioning.

# 3.1.2. Seaward dipping megasplay (backthrust) faults

The final states of simulations with the 45° seaward dipping megasplay fault show similar patterns of stress and strain to those with the landward dipping megasplay faults (Fig. 3). As shown in Fig. 3a-d,  $\sigma_m$ decreases across the inner wedge and rises near the boundary with the VS outer wedge during earthquake unloading. Fig. 3a–d shows that the area of reduced  $\sigma_m$  (cold color region) also decreases as the ratio of the outer wedge to full wedge length (azure dashed lines) decreases. In particular, when the outer wedge is very small (Fig. 3d), the stress decreases throughout the entire wedge, demonstrating wholesale stress drop and wedge relaxation during the earthquake. However, in contrast to the models with landward megasplay faults (Fig. 2e and h), there is no evidence of a normal sense of shear along any of the seaward dipping megasplay faults, even in the cases with very small outer wedge ratios (<15%) shown in Fig. 3g and h. Interestingly, the presence of larger outer wedges (VS zone) sometimes causes the formation of new landward dipping thrust faults (Fig. 3e).

Plots of  $\sigma_1$  vectors on the cumulative change in  $\sigma_m$  and the final distortional strain invariant field for the seaward dipping splay faults (Fig. S3 in supplemental materials), show similar trends as observed for landward dipping faults (Fig. S2). The  $\sigma_1$  vectors decrease in magnitude and become sub-horizontal with decreasing width of the VS outer wedge. Furthermore, the coseismic activity of the seaward dipping splay

fault does not significantly partition stresses during the earthquake unloading (areas highlighted by red circles in Figs. S3g-S3j).

# 3.2. Effect of outer wedge width on seafloor displacement

We measure seafloor uplift for each simulation by comparing the preearthquake and final wedge surface, using vertical displacement of the wedge surface. This uplift, presumed to occur during the earthquake, is a direct indicator of tsunami potential. We apply a median filter to smooth perturbations in the uplift distribution introduced by the discrete nature of the DEM particle assemblage. The result reveals systematic variations in uplift that correlate with variations in the outer wedge width (Fig. 4). Horizontal seafloor displacement is calculated similarly, and is presented in the supplementary materials (Fig. S4). For both landward and seaward dipping splay faults, the thickest part of the wedge, located between the downdip limit and 160 km, exhibits subsidence (negative uplift, orange boxes in Fig. 4a and b), which decreases progressively in the seaward direction.

Fig. 4a and b shows slight variations in the uplift profiles in the vicinity of the splay faults (at about 50 km). However, the greatest variations occur in association with the width of the outer wedge. The largest outer wedge width results in significantly reduced seafloor uplift near the toe, whereas seafloor uplift progressively increases with decreasing outer wedge width, and the peak in the uplift shifts towards the toe (Fig. 4a and b). The final horizontal displacement of the seafloor correlates directly with the vertical displacement (Fig. S4). In general, the width of the velocity strengthening outer wedge is anticorrelated to both vertical and horizontal displacement, implying that the width of the outer wedge plays a key role in tsunami potential.

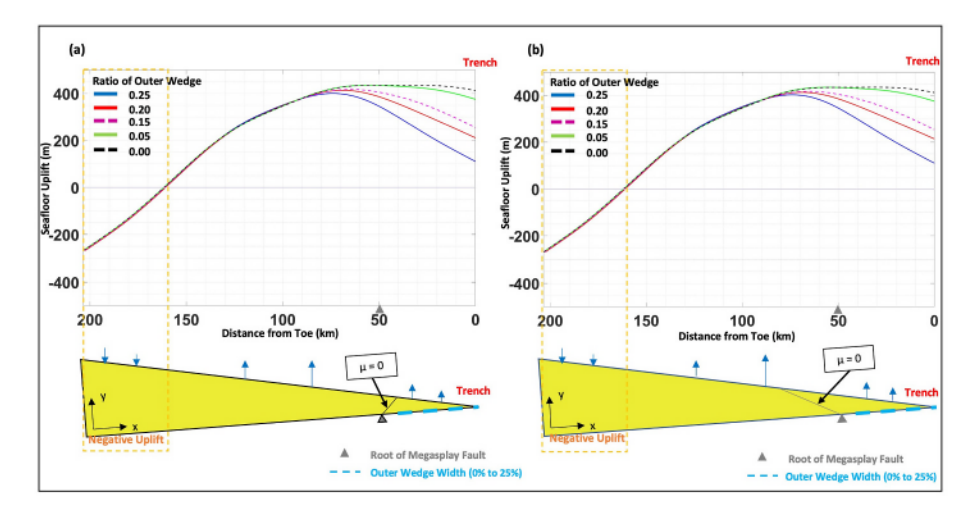


Fig. 4. Effect of outer wedge width on seafloor uplift. (a) Seafloor uplifts for 45° landward splay fault dip. (b) Seafloor uplifts for 45° seaward splay fault dip. Azure dashed lines represent outer wedge widths. Gray triangles indicate roots of splay faults.

### 3.3. Effect of megasplay fault dip on strain and seafloor displacement

The second set of simulations using Setup 1 was conducted for two fixed outer wedge widths at 0% and 25% of the full wedge width and with different splay fault orientations. The distortional strain invariant fields are plotted in Fig. 5 for cases with 0% outer wedge and Fig. 6 for those with 25% outer wedge. The  $\sigma_1$  vector for each case is also derived and plotted in Fig. S5 and Fig. S6 (supplemental materials).

Two reference models are shown without splay faults (Figs. 5a and 6a). In the case of no outer wedge (Fig. 5a), small normal-type shear zones are evident at very shallow depths and close to the wedge toe, indicating extension across the wedge. In the case of the 25% outer wedge (Fig. 6a), a small forethrust developed at the outer to inner wedge transition (~50 km).

As a result of earthquake unloading, megasplay faults within the wedges with no outer wedge essentially experienced limited shear strain (Figs. 2h, 3h and 5e), i.e., no coseismic activation (Fig. 5b–d, 5f, and 5g). Consequently, the  $\sigma_1$  vectors in the vicinity of the pre-existing megasplay fault plane are similar for all cases (Fig. S5 in supplementary materials). In contrast, megasplay faults within the models with the large outer wedges all exhibited some coseismic activation (Figs. 2e, 3e and 6b to 6g). Moreover, all landward dipping splay faults were all activated as thrust faults (Fig. 2e and 6b to 6d). Interestingly, the seaward dipping splay faults (Fig. 3e and 6e to 6g) also exhibit apparent activation as thrust faults. Essentially, the models with prescribed megasplay faults show different degrees of activation depending on outer wedge width. However, the activity of the megasplay fault and its dip, in general, have a limited effect on the  $\sigma_1$  vector.

Seafloor uplift for each case is shown in Fig. 7. In general, seafloor uplift for models with landward splay faults (Fig. 7a and c) and with seaward splay faults (Fig. 7b and d) are essentially identical. Zooming in to the regions near the wedge toes (black rectangles in Fig. 7), we observe that the curves for models with landward dipping splay faults are slightly separated near the wedge toes (Fig. 7a). In contrast, the curves for the models with seaward dipping splay faults essentially overlap (Fig. 7b and d). Compared to the outer wedge width (Fig. 4), the dip of the megasplay fault has a limited effect on seafloor uplift.

The horizontal seafloor displacement is also derived for each case (Fig. S7 in supplemental materials). As the geometry of the simulated slope surface is much simpler than the nature seafloor surface, the horizontal displacement is consistently larger than, but broadly correlated with, the vertical displacement. Again, the horizontal displacement of the models with landward dipping megasplay faults (Figs. S7a and S7c) and the ones with seaward dipping megasplay faults (Figs. S7b and S7d) are very comparable (Fig. S7), and thus we conclude that the

variation in geometry of the splay fault has little effect on the tsunami potential.

In summary, the width of the VS outer wedge controls the seafloor displacement near the wedge toe predominantly, whereas the effect of the megasplay fault dip is limited.

#### 4. Applications to the Maule and Tohoku earthquakes

We used Setup 2 to refine our previous simulations that sought to match published slip distributions for the 2010 Maule earthquake (Moreno et al., 2012; Wang et al., 2020) and 2011 Tohoku earthquake (Sun et al., 2017), respectively. Our previous investigation showed that the magnitude of peak fault slip has an inverse relationship with the outer wedge (Wang et al., 2021). That study also provided important constraints for the best-fit widths of the outer wedges in each location, and we use similar values for this study. Therefore, our coseismic slip distributions for simplified models with no splay faults (black dotted curves in Figs. 8 and 9) yield consistent peak slip values with those obtained for the Maule and Tohoku coseismic segments (Wang et al., 2021). Here, we investigate the influence of the megasplay faults on the coseismic rupture extents and tsunami potential. We conduct multiple simulations, prescribing splay faults with different friction coefficients (Table S1) before the start of the earthquake unloading stage. The cumulative change in  $\sigma_m$  and the corresponding  $\sigma_1$  vector are also plotted for all of the cases in Figs. S8 and S9 (supplementary materials).

# 4.1. 2010 Maule earthquake

Previous interpretations based on the tomographic model for the 2010 Mw 8.8 Maule earthquake rupture segment (Contreras-Reyes et al., 2010, 2017) show the outer wedge zone to be relatively large. The derived slip distributions for the 2010 Maule earthquake (Moreno et al., 2012; Wang et al., 2020) are shown in the pink band and dashed curve in Fig. 8b. The modeled peak slip is nearly 20 m and is located ~90 km from the trench. Our simulation without a splay fault reproduces this peak and its position reasonably well (black dotted curve in Fig. 8b). We then introduce an 80° seaward dipping splay fault that resembles the thrust-type Santa Maria fault system in the Maule segment (Fig. 8a). Based on the interpreted profile by Melnick et al. (2012), the root of the splay fault presumably overlaps the updip end of the seismogenic zone (inner wedge). The friction coefficient along the splay fault is unknown, so different values are tested in these simulations.

As shown in Fig. 8b to c, the presence of a pre-existing high-angle splay fault with any friction coefficient has minimal effect on the earthquake slip distribution. Likely, the large outer wedge (VS zone) in

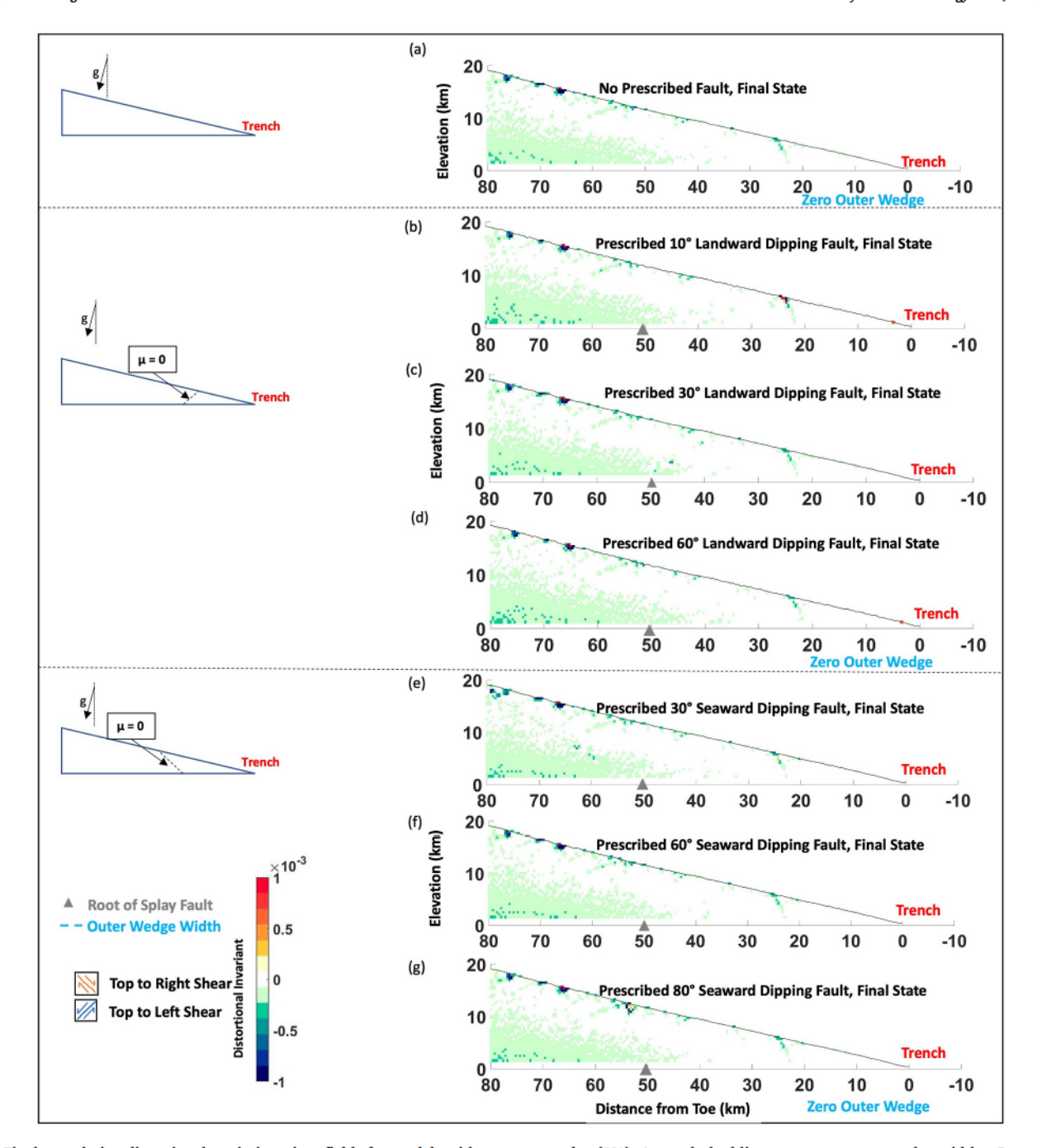


Fig. 5. Final cumulative distortional strain invariant fields for models with no outer wedge (0%). Azure dashed lines represent outer wedge widths. Gray triangles indicate roots of splay faults.

the Maule rupture zone (Contreras-Reyes et al., 2010; Wang et al., 2021) reduces fault activation and suppresses associated changes in slip. This transition zone between the inner and outer wedges results in a newly-formed compressive regime, reflected by the increased  $\sigma_m$  regions (warm color regions in Figs. S8c, S8e, S8g, and S8i) during the earth-quake unloading, causing localized uplift and subsidence (Fig. 8d). All of the models exhibit a prominent zone of high slip as well as large seafloor displacement at ~90 km (Fig. 8b–e), which is attributed to the change in friction condition at the boundary between the outer and inner wedge.

The activity of the megasplay fault affects the stress state after the earthquake, as reflected by the cumulative change in  $\sigma_m$  (warm color regions highlighted by green circles in Figs. S8b, S8d, S8f, and S8h). The increase in  $\sigma_m$  is inversely correlated to the amount of shear strain that occurred along the megasplay fault (regions in green circles in Fig. S8),

implying the activity of the splay fault accommodates some of the newly-formed compressive stress regimes. For the model with the lowest value of the friction along the splay fault, the deep section of the splay fault is also activated (region highlighted by the red box in Fig. S8b). As the value of friction on the megasplay fault increases, the shear strain along it decreases (highlighted by the red box in Figs. S8b, S8d, and S8f). Uplift of the hanging wall (<90 km), and subsidence of the footwall (>90 km) also decreases: it is greatest for the lowest values of friction (Fig. 8e), and most pronounced above the footwall.

The differences among the curves for the horizontal seafloor displacement (blue shading in Fig. 8e) are more apparent than for the vertical displacement (yellow shading in Fig. 8e), implying that the horizontal displacement may be more sensitive to the friction coefficient and activity of the megasplay fault. In general, the horizontal seafloor

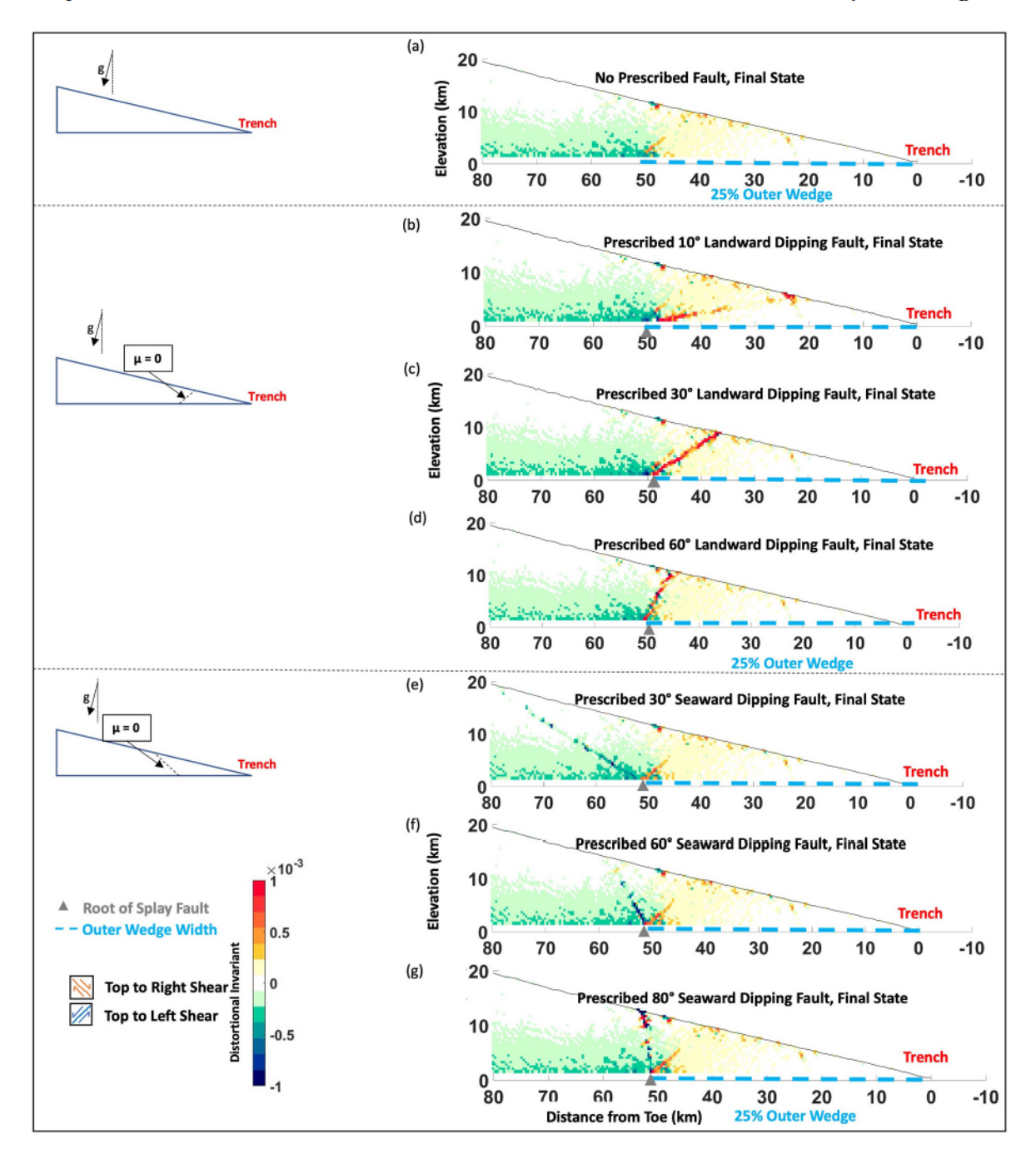


Fig. 6. Final cumulative distortional strain invariant fields for models with large outer wedges (25%). Colors and symbols are the same as in Fig. 5. (For interpretation of the references to color in this figure legend, the reader is referred to the Web version of this article.)

displacement is about twice that of the vertical displacement Thus, the horizontal seafloor displacement may be a key contributor to the tsunami genesis. However, the coseismic slip and seafloor displacement are predominantly controlled by the large outer wedge in the Maule rupture segment (Fig. 8b and d). To sum up, our simulation results suggest that the effect of the splay fault activity on the tsunami potential is relatively insignificant in the Maule rupture segment.

# 4.2. 2011 Tohoku earthquake

The 2011 Tohoku earthquake rupture segment is known to have experienced a trench breaking rupture with over 60 m peak slip (Sun et al., 2017; Wei et al., 2012). According to previous studies, a landward splay fault was reactivated by the 2011 Tohoku earthquake (Tsuji et al.,

2011). We, therefore, construct a model with a landward splay fault and a very small outer wedge (Fig. 9a), based on the published seismic profile by (Ito et al., 2011; Tsuji et al., 2011). Our model without a splay fault (black dotted curve in Fig. 9b) yielded a peak slip of about 64 m close to the trench, which is reasonably consistent with the derived slip distributions (pink band and dashed curve in Fig. 9b) for the 2011 Tohoku earthquake (Sun et al., 2017; Wang et al., 2021).

We also explore here how the presence of a landward dipping splay fault might affect the rupture extent and tsunami size. We fix the fault dip at 30°, comparable to the seismic interpretation (Tsuji et al., 2011), and examine different friction values along the fault. Fig. 9c shows that the coseismic megathrust fault slip and its amplitude are affected moderately by the friction along the splay fault. The separation between the model without a splay fault (black dotted curve in Fig. 9c) and the

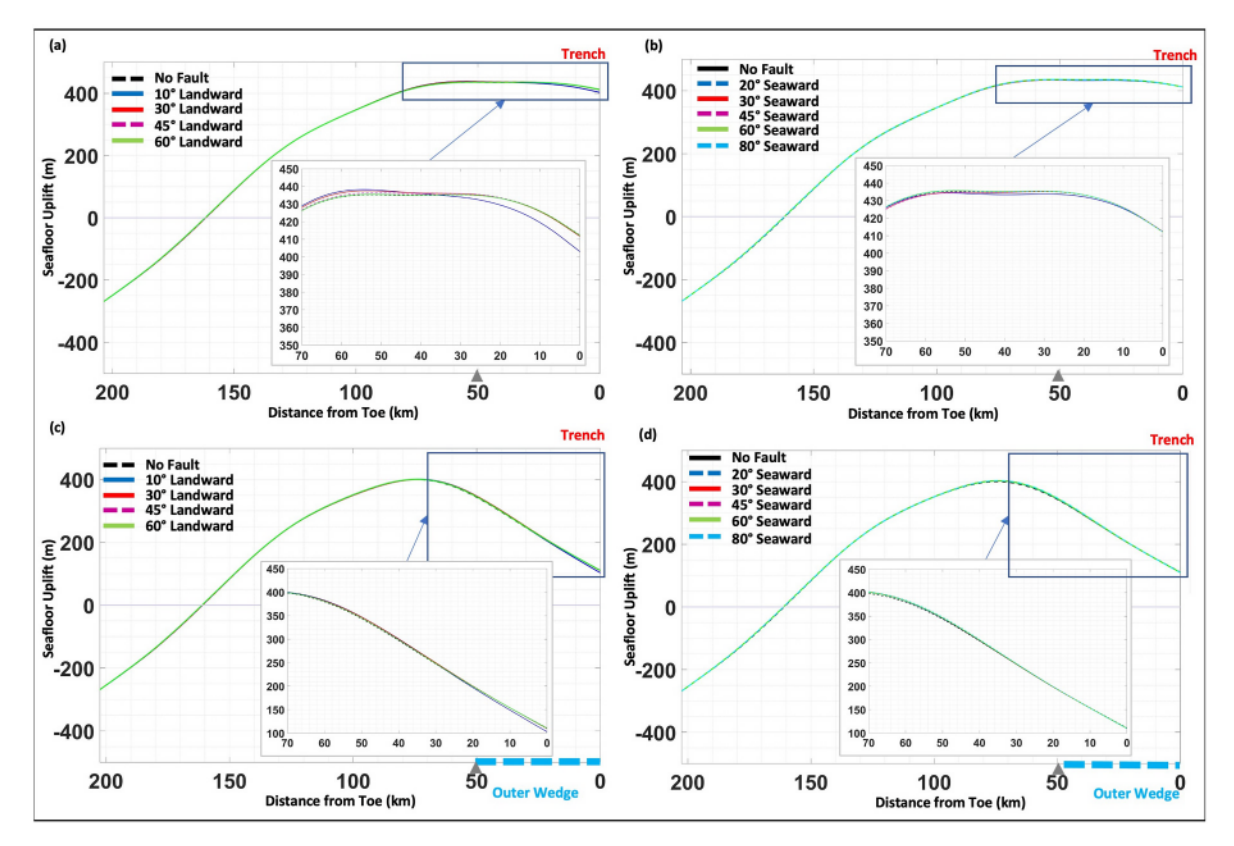


Fig. 7. Effect of splay fault dips on seafloor uplift. (a) Seafloor uplift for models with landward splay faults without an outer wedge. (b) Seafloor uplift for models with seaward splay faults without an outer wedge. (c) Seafloor uplift for models with landward splay faults with large outer wedges. (d) Seafloor uplift for models with seaward splay faults with large outer wedges. Azure dashed lines represent outer wedge dimension. Gray triangles locate roots of splay faults.

various faulted models (blue, red, and green curves in Fig. 9c) demonstrates that displacement along the splay fault (also highlighted by the red box in Figs. S9b, S9d, and S9f) can accommodate some of the coseismic slip along the decollement.

The dynamic weakening that occurred beneath the wedge gives rise to stress drop (cold color regions in Figs. S9c, S9e, S9g, and S9i), implying that the rupture has propagated all the way to the trench. The shear strain along the pre-existing fault mainly takes place at shallow depths as a result of the lower pre-consolidation stresses of shallow sediments, resulting in lower bulk strengths (Figs. S9b, S9d, and S9f). To some extent, the activity of the megasplay fault influences the stress state at the boundary between the outer and inner wedge after the earthquake. This is reflected by the cumulative change in  $\sigma_m$  (cold color regions highlighted by yellow circles in Figs. S9c, S9e, S9g, and S9i). The decrease in  $\sigma_m$  is inversely correlated to the shear strain that occurred along the megasplay fault (regions in yellow circles in Fig. S9).

Furthermore, our simulation results show that the coseismic displacement of the megasplay fault has a moderate effect on both vertical (yellow shading in Fig. 9d) and horizontal displacement (blue shading in Fig. 9d) near the wedge toe. Lower friction values along the splay fault correspond with increased uplift of the hanging wall of the landward splay fault during earthquake unloading (yellow shading in Fig. 9e). In general, the horizontal seafloor displacement is about three times more than vertical in the offshore forearc (Fig. 9e), again confirming that the horizontal seafloor displacement plays a key role in the tsunami genesis. The differences among the curves for horizontal seafloor displacement are more apparent than for vertical displacement (Fig. 9e), indicating that the horizontal displacement is more sensitive to the friction coefficient of the megasplay fault (forethrust) in the Tohoku area.

#### 5. Discussion

# 5.1. Relationship among outer wedge width, splay fault activity, and tsunami potential

Previous studies show the strong control of the width of the outer wedge (VS zone) on the rupture extents and slip distribution (Contreras-Reyes et al., 2010; Wang et al., 2021). Consistent with that finding, our first set of simulations of non-cohesive models also demonstrates that the width of the VS outer wedge affects the stress and strain along the splay fault (Figs. 2 and 3). Likely, different splay fault activities along different rupture segments triggered by the same seismic event (Lieser et al., 2014) are due to variations in outer wedge width along the margin. The width of the outer wedge gradually increases from south to north of the Maule segment along the SC Chile Margin (Contreras-Reyes et al., 2017). Splay fault activity during the 2010 Maule earthquake also appears to have increased from south to north (Lieser et al., 2014), which is consistent with our numerical results (Fig. 2e-g). Therefore, our numerical simulation suggests that the width of the outer wedge correlates with the activity of the pre-existing fault in the Maule rupture segment.

Furthermore, our analysis of the seafloor displacement (Fig. 4 and Fig. S4) shows that, to the first order, the width of the outer wedge may inversely correlate with the seafloor displacement. Interestingly, a normal splay fault can be activated during a megathrust earthquake if the outer wedge is sufficiently small. However, the amount of displacement on a normal fault is lower than on thrust splay faults (Figs. 2 and 3). Therefore, if significant thrust activity occurs along a splay fault, this may imply the presence of a wide outer wedge, reducing the tsunami potential locally (Fig. 4 and Fig. S4).

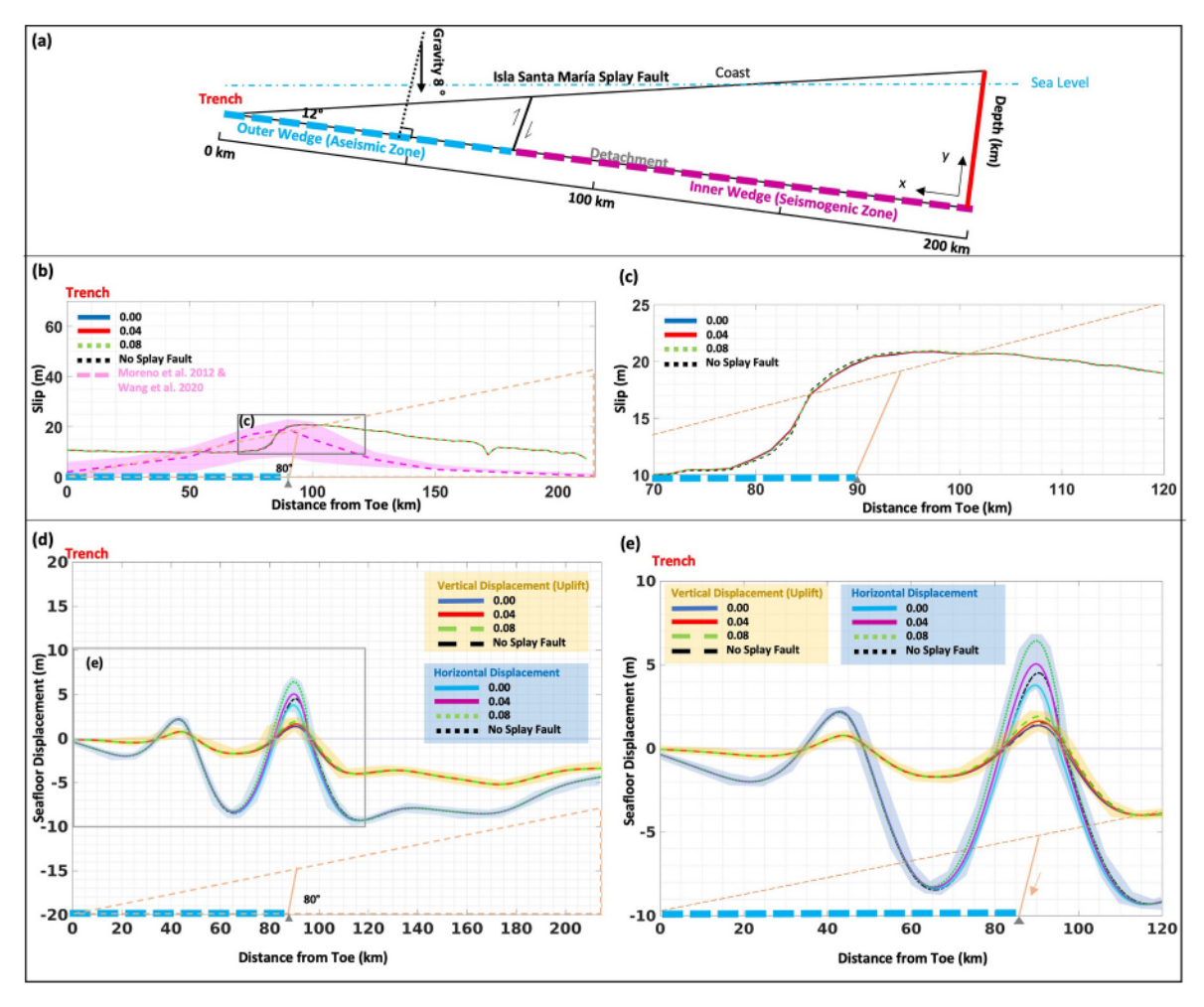


Fig. 8. Coseismic rupture and seafloor displacement for 2010 Maule earthquake from simulations. (a) Initial wedge setup (before the preconditioning stage) resembles wedge profile with the crustal structure of Santa Maria Fault System in SC Chile Margin near 2010 Maule earthquake (Melnick et al., 2012). Wedge supports an 80° seaward splay fault and large outer wedge. (b) Simulated slip distributions, compared to a range of slip models from Wang et al. (2020) shown in pink shading. (c) Enlargement of slip distributions within gray box shown in (b). (d) Simulated seafloor displacement. (e) Enlargement of displacement within gray box shown in (d). Dashed orange lines show geometry of upper plate, and solid orange line denotes position of splay fault plane. Yellow shading highlights vertical seafloor displacement, and blue shading highlights horizontal seafloor displacement. (For interpretation of the references to color in this figure legend, the reader is referred to the Web version of this article.)

# 5.2. Effects of megasplay fault properties on seismic hazard

Based on our first set of simplified models using different splay fault dips with the same values of fault friction, we demonstrate that variations in dip have a minimal effect on the stress and strain along the splay fault during the unloading phase (Fig. 5 and Fig. 6). Moreover, we see relatively insignificant differences in the seafloor displacement (Fig. 7). Thus, compared to the width of the outer wedge, variations in megasplay fault dip are unlikely to significantly affect tsunami potential during one seismic event. This can be explained by the limited amount of coseismic slip along the splay fault during one earthquake unloading event. The activity of the megasplay fault resulting from one seismic event does not result in significant stress partitioning across the splay fault either. Significantly greater cumulative displacement is necessary to detect such stress partitioning (Morgan, 2015). Furthermore, the preconditioning of the wedges results in similar initial stress states on the prescribed faults regardless of their orientation, limiting fault slip during unloading. If the splay faults have existed prior to the preconditioning, they might have accumulated different deformation and stress levels during loading, which could be reflected in differences in slip during the unloading (Morgan, 2015).

In our second set of models, however, we prescribe the splay faults

with fixed dips for each simulation case, and then test different values of friction coefficient along the splay fault. According to our simulation results for the 2010 Maule earthquake (Fig. 8), the dominant factor controlling the rupture extent and tsunami size is the width of the VS outer wedge. The simulation results show that the activity of the splay fault affects the postseismic stress state and slightly constrains the rise of  $\sigma_m$  at the boundary between outer and inner wedge. However, the width of the outer wedge (VS zone) is relatively large (Contreras-Reyes et al., 2010; Wang et al., 2021). The friction of the seaward splay fault, therefore, does not contribute much to the coseismic rupture extent and tsunami potential in the Maule rupture zone (Fig. 8b and d), and the coseismic displacements along the splay are very small.

Compared to the Maule rupture segment, the velocity strengthening outer wedge of the Tohoku rupture area is likely very small and allowed the wedge to experience trench breaking rupture (Ide et al., 2011; Ito et al., 2011; Wang and Tréhu, 2016). In our simulations, the friction on the megasplay fault and the corresponding activity have a moderate effect on the coseismic slip (Fig. 9b and c) and the horizontal displacement (blue shading in Fig. 9d and e). Our simulation results suggest that the main contributor of the tsunami potential is horizontal displacement (>50 m), which is consistent with the previous numerical studies (Song et al., 2017), and the evidence derived from the bathymetric (Fujiwara

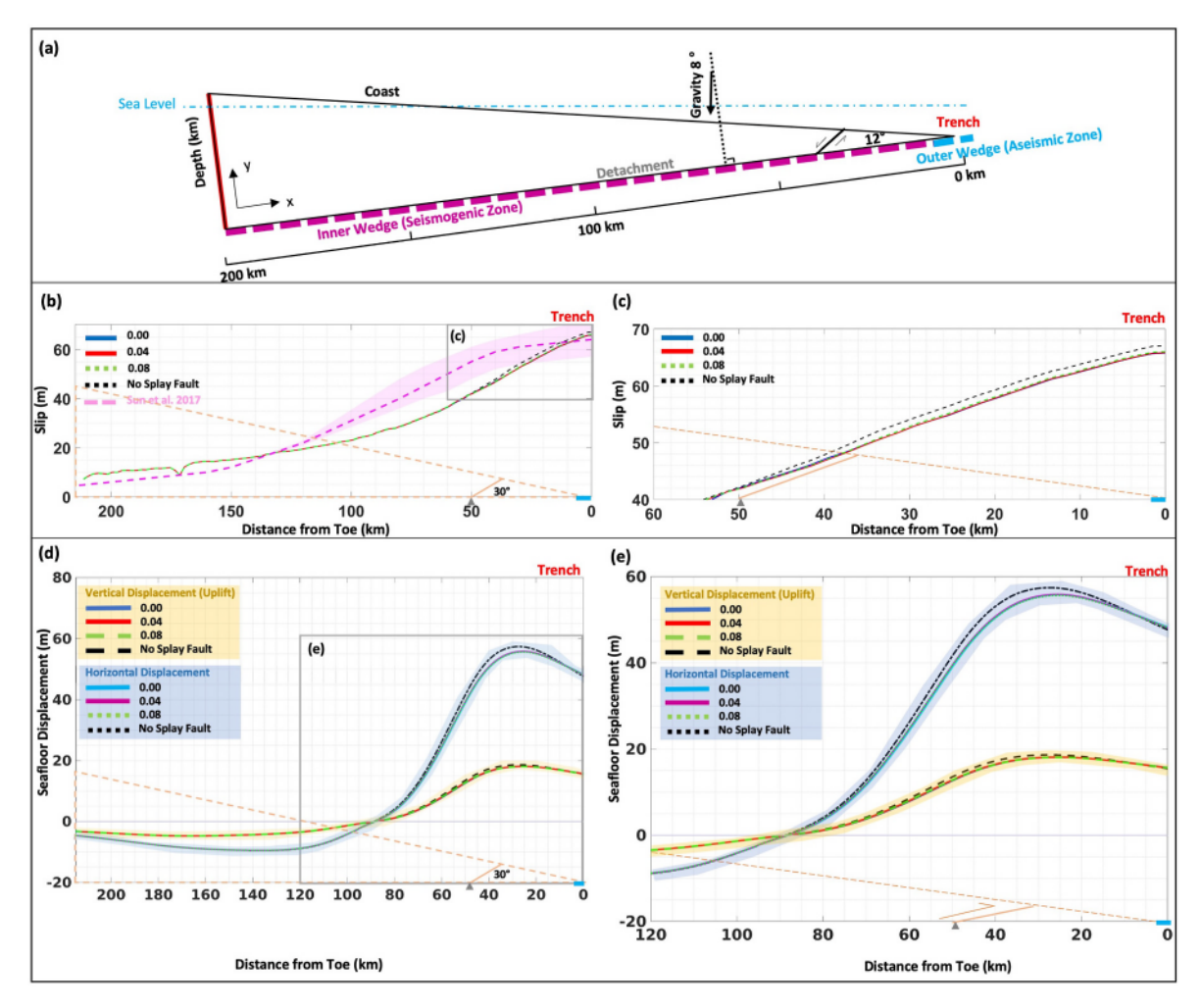


Fig. 9. Coseismic rupture and seafloor displacement for 2011 Tohoku earthquake from simulations. (a) Initial wedge setup, modeled after interpreted seismic reflection profile near 2011 Tohoku earthquake, with 30° landward splay fault and small outer wedge (Tsuji et al., 2011). (b) Simulated slip distributions, compared to preferred range of slip models from Sun et al. (2017) shown in pink shading. (c) Enlargement of slip distributions within gray box shown in (b). (d) Simulated seafloor displacement. (e) Enlargement of displacement within gray box shown in (d). The dashed orange lines show the geometry of the upper plate, and the solid orange line denotes the position of the splay fault plane. The yellow shading highlights the vertical seafloor displacement, and the blue shading highlights the horizontal seafloor displacement. (For interpretation of the references to color in this figure legend, the reader is referred to the Web version of this article.)

et al., 2011, 2017) and GPS (Sato et al., 2011) data. Compared to the horizontal seafloor displacement in the Maule rupture segment (Fig. 8e), the one in the Tohoku rupture segment (Fig. 9e) significantly contributes to the tsunami genesis. Therefore, the activity of the landward dipping splay fault may have affected the tsunami potential during the seismic event implicitly, supporting the seismic interpretation by Tsuji et al. (2011). This major difference between Maule and Tohoku rupture segments is very likely attributed to the width of the velocity strengthening outer wedge.

In summary, our simulation results demonstrate that the effects of megasplay faults during a single earthquake unloading event are limited. The presence of megasplay faults and their reactivation may not necessarily contribute to large earthquake size and tsunami potential. Likely, a more critical factor is the change in basal friction along the megathrust fault throughout one earthquake cycle. The properties of the splay fault are second-order factors that may moderately influence the rupture extents and tsunami size. If the VS outer wedge is small enough, the activity of the megasplay fault triggered by the earthquake, to some extent, contributes to the horizontal seafloor displacement, increasing the tsunami potential. In contrast, the seafloor displacement is constrained by a large VS outer wedge, implying small tsunami potential regardless of the activity of the megasplay fault. Therefore, this finding suggests that the coseismic normal fault slip in the Shumagin Gap may

not have played as significant a role in rupture extent or tsunami genesis as suggested by others (Bécel et al., 2017).

# 5.3. Other controlling factors for coseismic rupture and tsunami potential

Our simulated coseismic slip for the 2010 Maule segment and the simulated seafloor displacement (including both horizontal and vertical ones) are comparable to the published slip distribution (Moreno et al., 2012; Wang et al., 2020) and previous results derived from the bathymetric data for 2010 Maule rupture segment (Maksymowicz et al., 2017), respectively. Moreover, the simulated coseismic slip for the Tohoku earthquake is consistent with previous studies (Ito et al., 2011; Sun et al., 2017). In general, our simulated horizontal seafloor displacement for the Tohoku earthquake is large, indicating considerable tsunami potential for the 2011 Tohoku earthquake segment (Fujiwara et al., 2017; Ito et al., 2011).

In this study, we use a simplified 2D model to examine whether the width of the VS outer wedge, the presence of the megasplay fault itself, and their interactions are indicative of the local seismic risk and tsunami potential. Besides these two factors, there are still other pre-existing structural features and mechanical properties to be explored in the forearc, including the geometry of the accreted sediment close to wedge toe (Polet and Kanamori, 2000), backstop geometry (Kopp and

Kukowski, 2003), width and thickness of subducted sediments downdip (Olsen et al., 2020), basement morphology (Barker et al., 2018; Bilek et al., 2003; Morgan and Bangs, 2017), basal friction along decollement (Cubas et al., 2013), and internal friction within the wedge (Wang and Morgan, 2019). Nevertheless, our current models enable us to better understand how splay faults and frictional variations along the megathrust contribute to tsunami genesis and interact with other factors.

#### 6. Conclusions

We carried out two sets of simulations to examine the effects of splay fault dips on rupture extents and seafloor uplift. Our first set of simulations using non-cohesive models demonstrates that the width of VS outer wedge along the margin has the most significant effect on splay fault activity and thus on tsunami generation at different localities. The variations in outer wedge width (VS zone) along strike in the Maule rupture zone can help explain the various splay fault activities observed at different localities during the 2010 event.

In the second part of the study, we build more realistic cohesive models to assess the effects of splay faults on simulated megathrust displacements, which may better match published coseismic slip distributions for the 2010 Maule and 2011 Tohoku earthquakes. Different values of friction coefficient along the splay fault plane can lead to varying amounts of displacement along the splay fault during earthquake unloading. However, our simulation results indicate that the earthquake rupture extent and tsunami potential are predominantly controlled by friction variations along the megathrust fault, governed by outer wedge (VS zone) width, rather than friction along the megasplay fault. Our numerical results demonstrate that activation of a megasplay fault likely had minimal effect on earthquake coseismic rupture and tsunami potential during the 2010 Maule rupture, but could have had a moderate effect during the 2011 Tohoku rupture.

Our results show that the presence of megasplay normal faults does not necessarily imply significant seismic hazards in a subduction system. The effect of megasplay fault dip and its corresponding coseismic displacements along the splay fault on rupture extents and tsunami genesis is limited. We suggest that the properties of the splay fault are second-order factors affecting coseismic slip distribution and tsunami potential, whereas the critical factor is the variation in basal friction along the megathrust fault.

#### **Author statement**

Xiaoyu Wang: Writing – Original Draft, Software, Methodology, Formal analysis, Visualization, Investigation. Julia Morgan: Writing – Review & Editing, Funding acquisition, Supervision, Conceptualization, Software.

# Declaration of competing interest

The authors declare that they have no known competing financial interests or personal relationships that could have appeared to influence the work reported in this paper.

# Acknowledgments and Data

This work was funded in part by the National Science Foundation grant EAR-1723249. Computing facilities were made available in part through the Rice Center for Computational Geophysics. We thank two anonymous reviewers for their insightful comments and suggestions. The author benefitted from discussions about modeling and subduction systems with Dr. Gary Gray and my other colleagues. Interested parties are encouraged to contact the author to request copies of animated GIFs of the simulations for further study. The modeling results, corresponding files, raw data, and sample code for this research can be found at https://doi.org/10.6084/m9.figshare.15122229.v1.

#### Appendix A. Supplementary data

Supplementary data to this article can be found online at https://doi.org/10.1016/j,jsg.2022.104533.

#### References

- Barker, D.H., Henrys, S., Caratori Tontini, F., Barnes, P.M., Bassett, D., Todd, E., Wallace, L., 2018. Geophysical constraints on the relationship between seamount subduction, slow slip, and tremor at the north hikurangi subduction zone, New Zealand. Geophys. Res. Lett. 45 (12), 804-812,813.
- Bécel, A., Shillington, D.J., Delescluse, M., Nedimović, M.R., Abers, G.A., Saffer, D.M., Webb, S.C., Keranen, K.M., Roche, P.-H., Li, J., 2017. Tsunamigenic structures in a creeping section of the Alaska subduction zone. Nat. Geosci. 10, 609–613.
- Bilek, S.L., Schwartz, S.Y., DeShon, H.R., 2003. Control of seafloor roughness on earthquake rupture behavior. Geology 31, 455–458.
- Contreras-Reyes, E., Maksymowicz, A., Lange, D., Grevemeyer, I., Muñoz-Linford, P., Moscoso, E., 2017. On the relationship between structure, morphology and large coseismic slip: a case study of the mw 8.8 maule, Chile 2010 earthquake. Earth Planet Sci. Lett. 478, 27–39.
- Contreras-Reyes, E., Flueh, E.R., Grevemeyer, I., 2010. Tectonic control on sediment accretion and subduction off south central Chile: implications for coseismic rupture processes of the 1960 and 2010 megathrust earthquakes. Tectonics 29.
- Cubas, N., Avouac, J.-P., Leroy, Y.M., Pons, A., 2013. Low friction along the high slip patch of the 2011 mw 9.0 tohoku-oki earthquake required from the wedge structure and extensional splay faults. Geophys. Res. Lett. 40, 4231–4237.
- Dielforder, A., 2017. Constraining the strength of megathrusts from fault geometries and application to the alpine collision zone. Earth Planet Sci. Lett. 474, 49–58.
- Dieterich, J.H., 1979. Modeling of rock friction: 1. Experimental results and constitutive equations. J. Geophys. Res. Solid Earth 84, 2161–2168.
- Fujiwara, T., dos Santos Ferreira, C., Bachmann, A.K., Strasser, M., Wefer, G., Sun, T., Kanamatsu, T., Kodaira, S., 2017. Seafloor displacement after the 2011 tohoku-oki earthquake in the northern Japan trench examined by repeated bathymetric surveys. Geophys. Res. Lett. 44 (11), 833-811,839.
- Fujiwara, T., Kodaira, S., No, T., Kaiho, Y., Takahashi, N., Kaneda, Y., 2011. The 2011 tohoku-oki earthquake: displacement reaching the trench axis. Science 334, 1240-1240.
- Fulton, P., Brodsky, E.E., Kano, Y., Mori, J., Chester, F., Ishikawa, T., Harris, R., Lin, W., Eguchi, N., Toczko, S., 2013. Low coseismic friction on the tohoku-oki fault determined from temperature measurements. Science 342, 1214–1217.
- Grassi, B., 2021. Largest Earthquake in 50 Years: what We Know So Far. Alaska Earthquake Center earthquake alaska.edu.
- Ide, S., Baltay, A., Beroza, G.C., 2011. Shallow dynamic overshoot and energetic deep rupture in the 2011 mw 9.0 tohoku-oki earthquake. Science 332, 1426–1429.
- Ito, Y., Tsuji, T., Osada, Y., Kido, M., Inazu, D., Hayashi, Y., Tsushima, H., Hino, R., Fujimoto, H., 2011. Frontal wedge deformation near the source region of the 2011 tohoku-oki earthquake. Geophys. Res. Lett. 38.
- Kame, N., Rice, J.R., Dmowska, R., 2003. Effects of prestress state and rupture velocity on dynamic fault branching. J. Geophys. Res. Solid Earth 108.
- Kopp, H., Kukowski, N., 2003. Backstop geometry and accretionary mechanics of the sunda margin. Tectonics 22.
- Lieser, K., Grevemeyer, I., Lange, D., Flueh, E., Tilmann, F., Contreras-Reyes, E., 2014.
  Splay fault activity revealed by aftershocks of the 2010 mw 8.8 maule earthquake, central Chile. Geology 42, 823–826.
- Lotto, G.C., Dunham, E.M., Jeppson, T.N., Tobin, H.J., 2017. The effect of compliant prisms on subduction zone earthquakes and tsunamis. Earth Planet Sci. Lett. 458, 213–222.
- Lotto, G.C., Jeppson, T.N., Dunham, E.M., 2019. Fully coupled simulations of megathrust earthquakes and tsunamis in the Japan trench, nankai trough, and cascadia subduction zone. Pure Appl. Geophys. 176, 4009–4041.
- Maksymowicz, A., 2015. The geometry of the chilean continental wedge: tectonic segmentation of subduction processes off Chile. Tectonophysics 659, 183–196.
- Maksymowicz, A., Chadwell, C., Ruiz, J., Tréhu, A., Contreras-Reyes, E., Weinrebe, W., Díaz-Naveas, J., Gibson, J., Lonsdale, P., Tryon, M., 2017. Coseismic seafloor deformation in the trench region during the mw8. 8 maule megathrust earthquake. Sci. Rep. 7, 1–8.
- McKenzie, D., Jackson, J., 2012. Tsunami earthquake generation by the release of gravitational potential energy. Earth Planet Sci. Lett. 345, 1–8.
- Melnick, D., Bookhagen, B., Echtler, H.P., Strecker, M.R., 2006. Coastal deformation and great subduction earthquakes, isla santa maría, Chile (37 s). Geol. Soc. Am. Bull. 118, 1463–1480.
- Melnick, D., Moreno, M., Motagh, M., Cisternas, M., Wesson, R.L., 2012. Splay fault slip during the mw 8.8 2010 maule Chile earthquake. Geology 40, 251–254.
- Moore, G., Bangs, N., Taira, A., Kuramoto, S., Pangborn, E., Tobin, H., 2007. Threedimensional splay fault geometry and implications for tsunami generation. Science 318, 1128–1131.
- Moreno, M., Melnick, D., Rosenau, M., Baez, J., Klotz, J., Oncken, O., Tassara, A., Chen, J., Bataille, K., Bevis, M., 2012. Toward understanding tectonic control on the mw 8.8 2010 maule Chile earthquake. Earth Planet Sci. Lett. 321, 152–165.
- Moreno, M., Rosenau, M., Oncken, O., 2010. 2010 maule earthquake slip correlates with pre-seismic locking of andean subduction zone. Nature 467, 198–202.
- Morgan, J.K., 2015. Effects of cohesion on the structural and mechanical evolution of fold and thrust belts and contractional wedges: discrete element simulations. J. Geophys. Res. Solid Earth 120, 3870–3896.

- Morgan, J.K., Bangs, N.L., 2017. Recognizing seamount-forearc collisions at accretionary margins: insights from discrete numerical simulations. Geology 45, 635–638.
- Okamoto, A.S., Niemeijer, A.R., Takeshita, T., Verberne, B.A., Spiers, C.J., 2020. Frictional properties of actinolite-chlorite gouge at hydrothermal conditions. Tectonophysics 779, 228377.
- Olsen, K.M., Bangs, N.L., Tréhu, A.M., Han, S., Arnulf, A., Contreras-Reyes, E., 2020. Thick, strong sediment subduction along south-central Chile and its role in great earthquakes. Earth Planet Sci. Lett. 538, 116195.
- Park, J.-O., Tsuru, T., Kodaira, S., Cummins, P.R., Kaneda, Y., 2002. Splay fault branching along the nankai subduction zone. Science 297, 1157–1160.
- Polet, J., Kanamori, H., 2000. Shallow subduction zone earthquakes and their tsunamigenic potential. Geophys. J. Int. 142, 684–702.
- Rabinowicz, E., 1951. The nature of the static and kinetic coefficients of friction. J. Appl. Phys. 22, 1373–1379.
- Rabinowitz, H., Savage, H., Skarbek, R., Ikari, M.J., Carpenter, B.M., Collettini, C., 2018. Frictional behavior of input sediments to the hikurangi trench, New Zealand. Gcubed 19, 2973–2990.
- Ruppert, N.A., Gardine, L., 2021. 2020 alaska Seismicity Summary.
- Sato, M., Ishikawa, T., Ujihara, N., Yoshida, S., Fujita, M., Mochizuki, M., Asada, A., 2011. Displacement above the hypocenter of the 2011 tohoku-oki earthquake. Science 332, 1395-1395.
- Scholz, C.H., 1998. Earthquakes and friction laws. Nature 391, 37-42.
- Song, Y.T., Mohtat, A., Yim, S.C., 2017. New insights on tsunami genesis and energy source. J. Geophys. Res.: Oceans 122, 4238–4256.
- Sun, T., Wang, K., Fujiwara, T., Kodaira, S., He, J., 2017. Large fault slip peaking at trench in the 2011 tohoku-oki earthquake. Nat. Commun. 8, 1–8.
- Tong, X., Sandwell, D., Luttrell, K., Brooks, B., Bevis, M., Shimada, M., Foster, J., Smalley Jr., R., Parra, H., Báez Soto, J.C., 2010. The 2010 maule, Chile earthquake: downdip rupture limit revealed by space geodesy. Geophys. Res. Lett. 37.

- Tsuji, T., Ito, Y., Kido, M., Osada, Y., Fujimoto, H., Ashi, J., Kinoshita, M., Matsuoka, T., 2011. Potential tsunamigenic faults of the 2011 off the pacific coast of tohoku earthquake. Earth Planets Space 63, 58.
- Ujiie, K., Tanaka, H., Saito, T., Tsutsumi, A., Mori, J.J., Kameda, J., Brodsky, E.E., Chester, F.M., Eguchi, N., Toczko, S., 2013. Low coseismic shear stress on the tohoku-oki megathrust determined from laboratory experiments. Science 342, 1211–1214.
- Wang, K., Brown, L., Hu, Y., Yoshida, K., He, J., Sun, T., 2019. Stable forearc stressed by a weak megathrust: mechanical and geodynamic implications of stress changes caused by the m= 9 tohoku-oki earthquake. J. Geophys. Res. Solid Earth 124, 6179–6194.
- Wang, K., Hu, Y., 2006. Accretionary prisms in subduction earthquake cycles: the theory of dynamic coulomb wedge. J. Geophys. Res. Solid Earth 111.
- Wang, K., Huang, T., Tilmann, F., Peacock, S.M., Lange, D., 2020. Role of serpentinized mantle wedge in affecting megathrust seismogenic behavior in the area of the 2010 m= 8.8 maule earthquake. Geophys. Res. Lett. 47, e2020GL090482.
- Wang, K., Tréhu, A.M., 2016. Invited review paper: some outstanding issues in the study of great megathrust earthquakes—the cascadia example. J. Geodyn. 98, 1–18.
- Wang, X., Morgan, J.K., 2019. Controls on fore-arc deformation and stress switching after the great 2011 tohoku-oki earthquake from discrete numerical simulations. J. Geophys. Res. Solid Earth 124, 9265–9279.
- Wang, X., Morgan, J.K., Bangs, N., 2021. Relationships among forearc structure, fault slip, and earthquake magnitude: numerical simulations with applications to the central chilean margin. Geophys. Res. Lett. 48, e2021GL092521.
- Wei, S., Graves, R., Helmberger, D., Avouac, J.-P., Jiang, J., 2012. Sources of shaking and flooding during the tohoku-oki earthquake: a mixture of rupture styles. Earth Planet Sci. Lett. 333, 91–100.
- Wendt, J., Oglesby, D.D., Geist, E.L., 2009. Tsunamis and splay fault dynamics. Geophys. Res. Lett. 36.